GEOLOGY

The terrestrial end-Permian mass extinction in the paleotropics postdates the marine extinction

Qiong Wu[1,2], Hua Zhang[3], Jahandar Ramezani[4], Fei-fei Zhang[2], Douglas H. Erwin[5,6], Zhuo Feng[7,8], Long-yi Shao[9], Yao-feng Cai[3], Shu-han Zhang[2], Yi-gang Xu[1,10], Shu-zhong Shen[2]*

The end-Permian mass extinction was the most severe ecological event during the Phanerozoic and has long been presumed contemporaneous across terrestrial and marine realms with global environmental deterioration triggered by the Siberian Traps Large Igneous Province. We present high-precision zircon U-Pb geochronology by the chemical abrasion–isotope dilution–thermal ionization mass spectrometry technique on tuffs from terrestrial to transitional coastal settings in Southwest China, which reveals a protracted collapse of the Cathaysian rainforest beginning after the onset of the end-Permian marine extinction. Integrated with high-resolution geochronology from coeval successions, our results suggest that the terrestrial extinction occurred diachronously with latitude, beginning at high latitudes during the late Changhsingian and progressing to the tropics by the early Induan, spanning a duration of nearly 1 million years. This latitudinal age gradient may have been related to variations in surface warming with more degraded environmental conditions at higher latitudes contributing to higher extinction rates.

INTRODUCTION

The end-Permian mass extinction (EPME) was the most catastrophic of the Phanerozoic great mass extinctions (*1*). Most research has focused on the marine fossil records and perturbations to ocean chemistry, with far fewer studies of terrestrial and transitional coastal settings outside of classic regions such as South Africa (*2*). The majority of high-precision radioisotope geochronology constraining the timing and rates of the extinction is from marine sections in South China, which calibrate the onset of the marine EPME at 251.941 ± 0.037 million years (Ma) ago and as a brief event limited to 60 ± 48 thousand years (ka) (*3*) or possibly to 31 ± 31 ka (*4*). The favored trigger for this crisis has been the emplacement of the Siberian Traps Large Igneous Province (SLIP) based on their temporal overlap and coincident volcanic inputs indicated by geochemical proxies (*5*, *6*). This has led to the widespread assumption that the terrestrial and marine EPME were contemporaneous, with global environmental deterioration triggered by the SLIP as the primary cause (*7*, *8*). While a simultaneous crisis in marine and terrestrial ecosystems is the most parsimonious explanation, recent work has challenged this view as data from other regions indicated an earlier and protracted extinction in terrestrial high paleolatitudes (*9*–*13*). The temporal decoupling of marine and terrestrial extinctions requires a more complex extinction scenario. High-precision geochronology, especially from outside of the intensively studied marine paleotropics, is required to establish a high-resolution global timeline and test alternative models for relationships between environmental perturbations and the biological response.

The paleotropical terrestrial and transitional coastal deposits during the Permian-Triassic transition were widely developed in the western South China Block (Fig. 1), which are composed of the Xuanwei, Kayitou, and Dongchuan or Feixianguan formations in ascending order (Fig. 2 and the Supplementary Materials). The geological and biological events during the process of ecosystem collapse associated with the Permian-Triassic transition, including floral turnover, carbon cycle perturbations, wildfires, and volcanic events, have been widely studied in this area, which located the extinction interval within the nonmarine Kayitou Formation (Fig. 2) (*7*, *14*–*22*). The base of the Kayitou Formation is constrained by the disappearance of coal seams or the last appearance datum (LAD) of the organic-rich horizon (*16*), which also marks the demise of the Permian tropical forests and is thought to be correlative with the onset of the terrestrial EPME in other regions (*7*, *9*, *23*, *24*).

Despite its distinct lithostratigraphic and biostratigraphic characteristics, the temporal correlation of the Kayitou Formation has been controversial (*7*, *15*, *16*, *18*), hampering the EPME correlations across the paleotropical marine and terrestrial regions. Limited tuff zircon geochronology by in situ U-Pb analyses with errors >1% lacked the necessary resolution to constrain the Permian-Triassic boundary (PTB) or to address the timing of the terrestrial EPME in Southwest China (*25*, *26*). A legacy zircon U-Pb date by the chemical abrasion–isotope dilution–thermal ionization mass spectrometry (CA-ID-TIMS) method from the tuff inside the last coal (Bed 68) at the terrestrial Chahe section has been the only high-precision constraint for the tropical EPME on land (*7*). However, more recent CA-ID-TIMS geochronology using the EARTHTIME isotopic tracer solutions and analytical protocols are often younger than the legacy data (*3*), which makes the correlation between Bed 68 at the Chahe section and Bed 25 at the Meishan global boundary stratotype section and point (GSSP) ambiguous.

[1]Southern Marine Science and Engineering Guangdong Laboratory (Guangzhou), Guangzhou 511458, China. [2]State Key Laboratory for Mineral Deposits Research and School of Earth Sciences and Engineering, Nanjing University, Nanjing 210023, China. [3]LPS, Nanjing Institute of Geology and Palaeontology and Center for Excellence in Life and Paleoenvironment, Chinese Academy of Sciences, Nanjing 210008, China. [4]Department of Earth, Atmospheric, and Planetary Sciences, Massachusetts Institute of Technology, Cambridge, MA 02139, USA. [5]Department of Paleobiology, MRC-121, National Museum of Natural History, Washington, DC 20013-7012, USA. [6]Santa Fe Institute, 1399 Hyde Park Road, Santa Fe, NM 87501, USA. [7]Institute of Palaeontology, Yunnan Key Laboratory of Earth System Science, Yunnan Key Laboratory for Palaeobiology, MEC International Joint Laboratory for Palaeobiology and Palaeoenvironment, Yunnan University, Kunming 650500, China. [8]Southwest United Graduate School, Kunming 650092, China. [9]State Key Laboratory of Coal Resources and Safe Mining and College of Geoscience and Surveying Engineering, China University of Mining and Technology (Beijing), Beijing 100083, China. [10]State Key Laboratory of Isotope Geochemistry and Center of Excellence in Deep Earth Science, Guangzhou Institute of Geochemistry, Chinese Academy of Sciences, Guangzhou 510640, China.
*Corresponding author. Email: szshen@nju.edu.cn

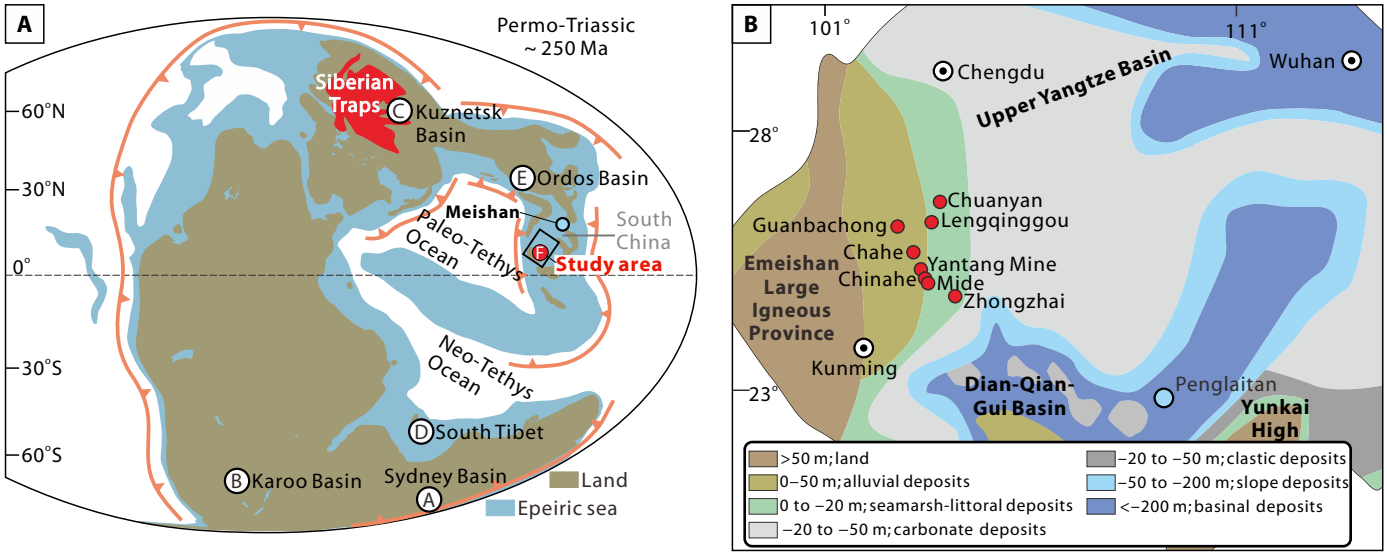

Fig. 1. Location of study area. (**A**) Reconstruction of Permo-Triassic paleogeography (*83*) showing the study area and sites of previous geochronological studies on the EPME. Schematic map of the Siberian Traps and coeval subduction zones are modified after (*84*) and (*21*). The box in (A) shows the location of the regional map (B). (**B**) Location of the studied sections in Southwest China (*7*).

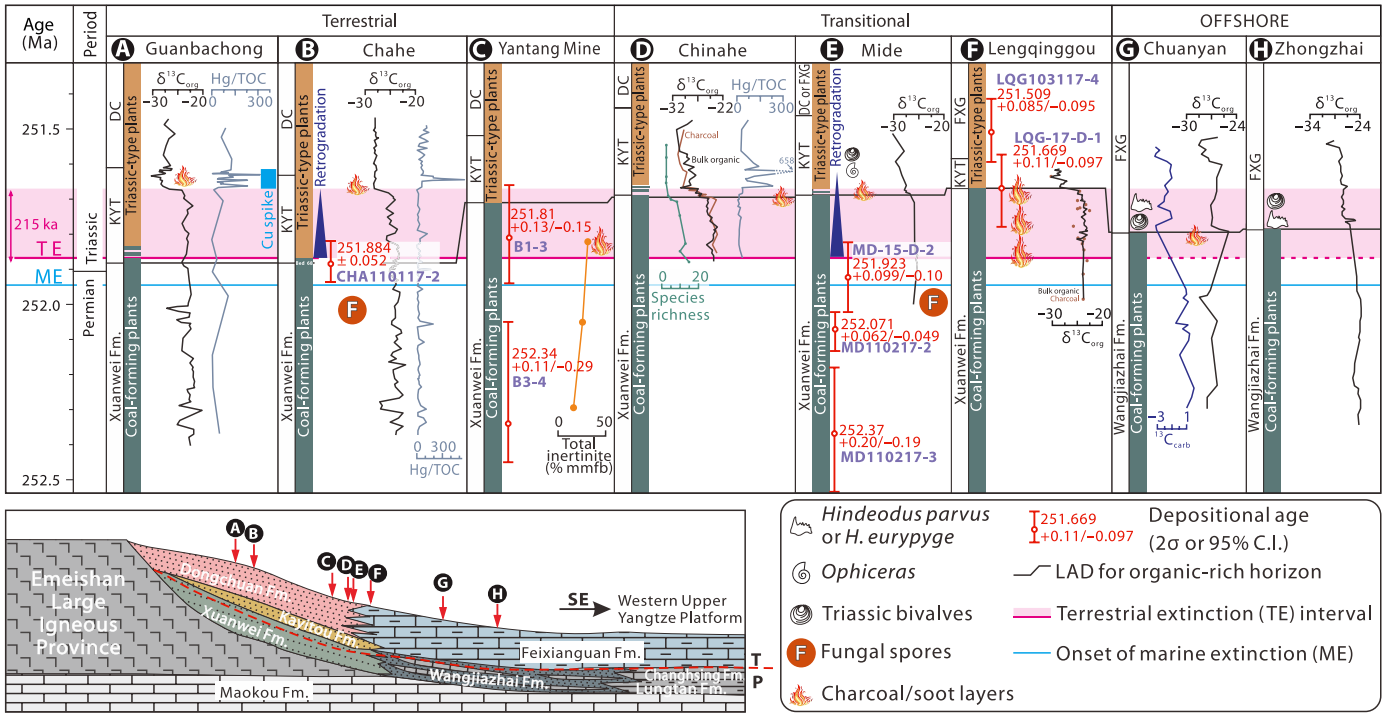

Fig. 2. Correlations of the EPME between terrestrial and transitional coastal sections in Southwest China. The floral turnover and environmental perturbations at the Guanbachong, Chahe, Yantang Mine, Chinahe, Mide, and Lengqinggou sections are extracted from (*14*, *16*–*21*, *66*). The carbon isotope profiles at the Chuanyan and Zhongzhai sections are from (*7*). Abbreviations: Fm., Formation; KYT, Kayitou Fm.; DC, Dongchuan Fm.; FXG, Feixianguan Fm.

Here, we present high-precision U-Pb zircon geochronology by the CA-ID-TIMS technique on a series of bentonites or tonsteins from terrestrial and transitional coastal Permian-Triassic successions in Southwest China to investigate the timing of the crisis in the terrestrial tropics. Our set of internally consistent and reproducible radioisotopic data allows direct comparison to previously reported CA-ID-TIMS geochronology in other regions for the EPME that followed the EARTHTIME protocols (*3*, *4*, *9*–*12*), effectively eliminating any interlaboratory bias. The integration of the available high-precision geochronology provides a global age model for the terrestrial ecosystem collapse. We tentatively estimated the latitudinal intensity of the terrestrial EPME based on fossil occurrence data from the

Paleobiology Database (PBDB), which suggests a lag in the crisis in terrestrial low latitudes accompanied by lower extinction rates.

RESULTS

Zircon U-Pb geochronology

Eight bentonite or tonstein samples for the zircon U-Pb geochronologic study were collected from the Chahe, Yantang Mine, Mide, and Lengqinggou sections ranging from onshore to paralic settings (Fig. 1). A total of 69 single-zircon U-Pb analyses from the eight samples were carried out by the CA-ID-TIMS technique (table S1). A number of our samples exhibit complex age spectra with resolvable excess scatter in the analyses (Fig. 3), possibly related to the presence of xenocrystic, antecrystic, or detrital zircons. Only in two cases can the outlier analyses be reliably excluded on the basis of discordance (MD110217-2: z3 and MD110217-3: z1). For the rest of the dataset, the date scatter is smaller than 0.8 Ma and thus cannot be objectively attributed to xenocrystic or detrital zircons. This complicates the estimation of eruptive age by the conventional weighted mean $^{206}Pb/^{238}U$ model for three of our samples (LQG-17-D-1, B1-3, and CHA110117-2) (table S3). For the latter ash beds, we have used a Bayesian Markov chain Monte Carlo (MCMC) algorithm proposed in (*27*) and acquired eruptive age estimates based on a range of predicted preeruptive age-mass distributions implemented in the Chron.jl package (*27*, *28*). Calculated ages from the MCMC algorithm, as well as those from the conventional weighted means of the youngest zircon populations and our preferred interpretations, are presented in table S3, Fig. 3, and fig. S6. Where appropriate, these eruptive ages were further refined through superposition by an MCMC rejection algorithm through the Bchron package (*29*) to generate an age-stratigraphic model for the corresponding sections (Table 1 and fig. S8).

The geochronology of the main marine extinction was previously established by the zircon U-Pb CA-ID-TIMS analyses from the Meishan GSSP (*3*) in South China, using similar analytical procedures as those in this study. Nevertheless, the previously published data were invariably interpreted on the basis of weighted mean $^{206}Pb/^{238}U$ dates of all or the youngest population of zircon analyses. Furthermore, the published age model for the Meishan GSSP was constructed on the basis of a simple (non-Bayesian) Monte Carlo simulation algorithm (*30*), which relied on the assumption of a constant sediment accumulation rate. Therefore, we revisited the previously published geochronology based on the same age interpretation approach as in this study. The resulting model age for the onset of the main marine mass extinction (Bed 25) at the Meishan GSSP is 251.945 ± 0.033 Ma ago, indistinguishable within error from the published age of 251.941 ± 0.037 Ma ago (Supplementary Text and table S4).

The mean square weighted deviation for sample CHA110117-2 is close to the upper limit for a statistically coherent set of U-Pb dates (table S3). Thus, both the conventional weighted mean model and a Bayesian MCMC model are used to interpret the U-Pb data for this sample, constraining the depositional age of Bed 68 associated with the last coal seam at the Chahe section to 251.884 ± 0.052 or 251.804 + 0.078/−0.10 Ma ago, respectively (Fig. 3 and Table 1). The last coal at the top of the Xuanwei Formation at the Lengqinggou section coincides with the last occurrence of the *Gigantopteris* flora at this section and is constrained to 251.669 + 0.11/−0.097 Ma ago based on the ages of two dated bentonites (LQG-17-D-1 and LQG103117-4) and the corresponding Bayesian age-stratigraphic model (Table 1). Sample B1-3 from the Yantang Mine section was collected from an ash bed immediately below the 30-cm-thick coal roof (the last coal) of the Xuanwei Formation, whose age constrains the base of the Kayitou Formation to younger than 251.81 + 0.13/−0.15 Ma old. At the Mide section, the youngest of the three dated beds (MD-15-D-2) from the Xuanwei Formation lies nearly 1 m below the LAD of the organic-rich horizon and yielded an age of 251.923 + 0.099/−0.10 Ma ago. This relationship prevents a direct U-Pb age constraint on the base of the Kayitou Formation in this location (see Discussion).

Latitudinal extinction intensity

We estimated the latitudinal genus extinction rates in terrestrial realms based on the data from the PBDB (table S10). The global weighted mean genus extinction rate for EPME is ~59% by comparing fossil occurrence data from the Changhsingian with those in the Induan (Fig. 4A and table S5). The observed extinction intensity increases by nearly 15% from ~53% in the low latitudes to ~68% in the

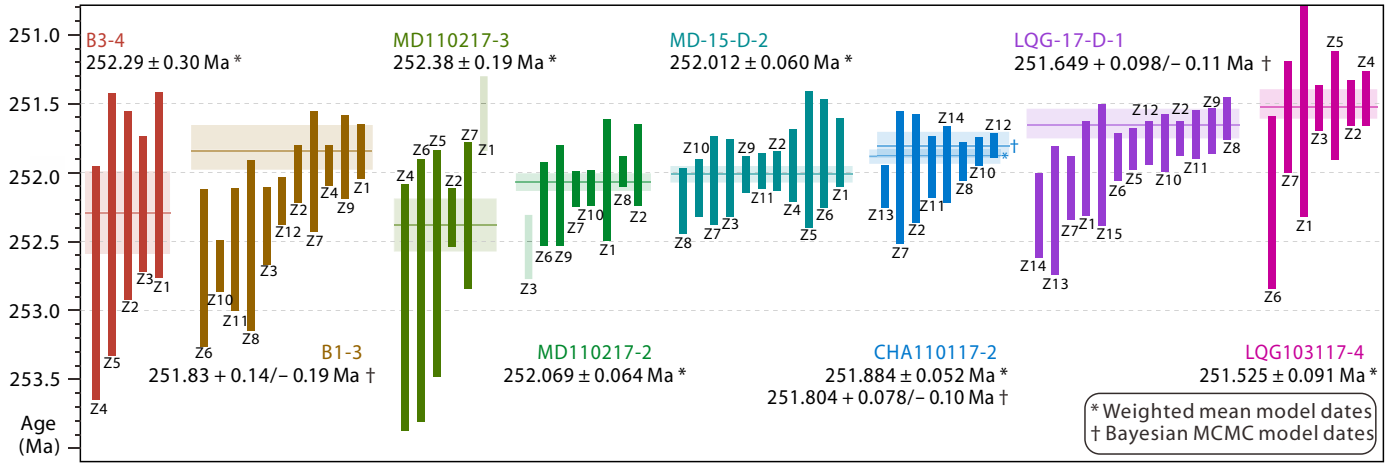

Fig. 3. $^{206}U/^{238}Pb$ age distribution of analyzed single zircons from tuffs in terrestrial and transitional coastal sections in Southwest China. Horizontal lines and shaded bands signify the estimated eruptive ages by the Bayesian MCMC algorithm with 95% confidence interval or the weighted mean model with 2σ error. The analyses of z1 from sample MD110217-3 and z3 from sample MD110217-2 were excluded from the calculation due to discordance.

Table 1. Summary of U-Pb eruptive and refined depositional ages.

		Eruptive age*		Model depositional age†	
		Mean age	Confidence level	Mean age	Confidence level
Sample‡	Section	(Ma)	(±95% or 2σ)	(Ma)	(±95%)
CHA110117-2	Chahe	251.884	±0.052	-	-
CHA110117-2	Chahe	**251.804**	**+0.078/−0.10**	-	-
B1-3	Yantang Mine	**251.83**	**+0.14/−0.19**	251.81	+0.13/−0.15
B3-4	Yantang Mine	252.29	±0.30	252.34	+0.11/−0.29
MD-15-D-2	Mide	252.012	±0.060	251.923	+0.099/−0.10
MD110217-2	Mide	252.069	±0.064	252.071	+0.062/−0.049
MD110217-3	Mide	252.38	±0.19	252.37	+0.20/−0.19
LQG103117-4	Lengqinggou	251.525	±0.091	251.509	+0.085/−0.095
LQG-17-D-1	Lengqinggou	**251.649**	**+0.098/−0.11**	251.669	+0.11/−0.097

*Eruptive ages in bold are estimated on the basis of a Bayesian MCMC algorithm (*27*), otherwise derived from the weighted mean $^{206}Pb/^{238}U$ dates. †Model depositional ages are estimated on the basis of an MCMC age-stratigraphic algorithm (*29*, *85*). ‡Eruptive ages for sample CHA110117-2 generated by the weighted mean and MCMC models are both displayed.

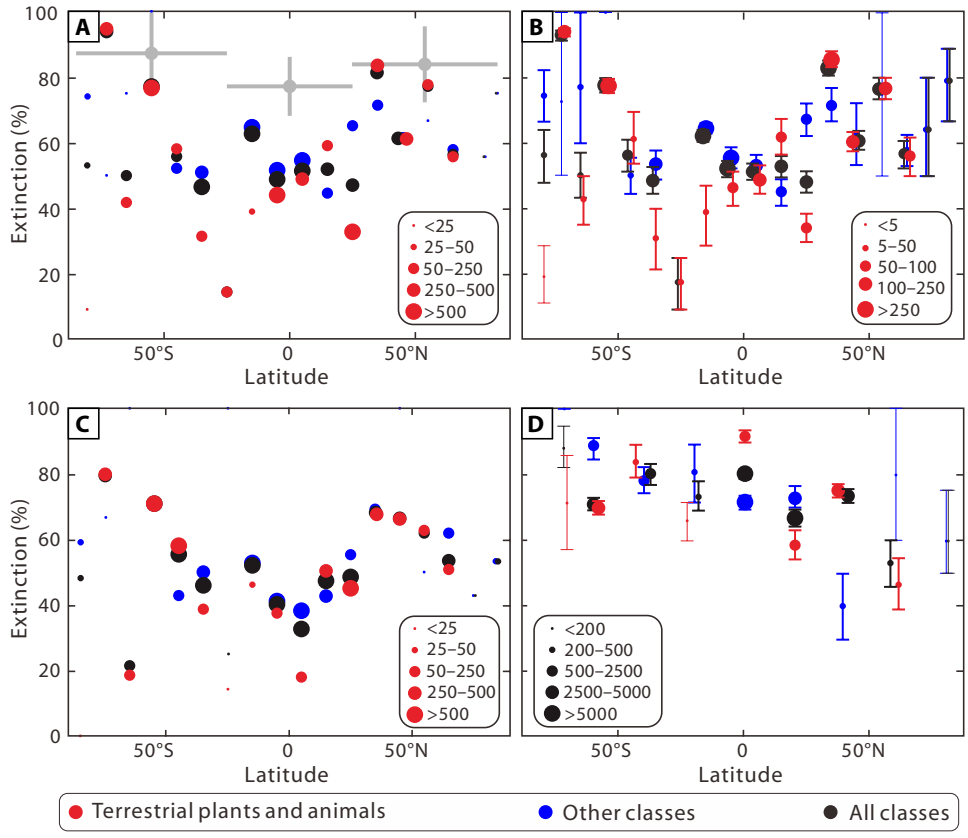

Fig. 4. Latitudinal end-Permian genus extinction pattern based on fossil occurrence data in PBDB. (**A**) Estimation based on data from Changhsingian to Induan. Observed extirpation magnitudes (gray points) are averaged across tropical and extratropical latitude bands (gray horizontal lines) with gray vertical bars showing 1σ SDs. (**B**) Estimation based on data from Changhsingian to Induan by bootstrap analyses. Vertical bars show the confidence interval within 10 to 90% quantile ranges. (**C**) Estimation based on data from Changhsingian to the entire Triassic. (**D**) Estimation based on data from Wuchiapingian to Olenekian by the GF method. Symbol size in (A) to (C) is scaled by the number of fossil occurrences in Changhsingian and in (D) by the total number of fossil occurrences from Wuchiapingian to Olenekian.

middle and high latitudes. The results from the bootstrap analyses on the same fossil occurrence dataset fit well with the raw data (Fig. 4B and table S6). The observed uncertainties are relatively large in high latitudes due to the limited number of samples. The fossil extirpation intensities are more severe than the extinction intensities across all latitudes with a global mean rate of ~81%, but they also show a similar gradient outside of the tropics (Fig. 4A).

To account for the Signor-Lipps and edge effects, we applied the Gap-filler (GF) method proposed by Alroy (*31*, *32*) to the Wuchiapingian to Olenekian dataset to calculate the extinction intensity. Most of the latitudinal extinction rates are between about 59 and 88% with a weak gradient from high to low latitudes, except for a high extinction rate for the terrestrial plants and animals in the band of 10°S to 10°N (Fig. 4D and table S7). Greater variability and uncertainty in the extinction rates are observed in northern high latitudes, which may have been attributed to limited number of samples. The GF method was originally designed to assess global diversity patterns. When applied to latitudinal binned data, the extinction rates can be influenced by long-term migrations or local extirpation, which generates higher extinction intensity across all latitude bands. Therefore, the GF method may not function as effectively as intended in this context. We also estimated the extinction intensity by comparing data from the Changhsingian with those from the entire Triassic (Fig. 4C and table S8). A lower global weighted mean average genus extinction rate for the EPME (~51%) is observed, which we attributed to the incomplete preservation of some survivors during the Induan. Despite that, the extinction intensity shows an increase of ~16% from the tropics (~44%) to the middle and high latitudes (~60%). In summary, the fossil occurrence dataset of PBDB suggests lower extinction rates in terrestrial low latitudes during the Permian-Triassic transition despite the relatively large errors in high latitudes.

DISCUSSION

Calibration of the EPME in terrestrial paleotropics

Extending the high-resolution tempo of the EPME to terrestrial realms yields insights into the dynamics of this event. Understanding the pace of extinction in terrestrial regions is inherently more complicated than in shallow marine settings: Vertebrates are less abundant, and thus, their fossils are sparser, enhancing the Signor-Lipps effect, and many terrestrial organisms are more difficult to preserve. These factors highlight the importance of radioisotopic data and chemostratigraphy in resolving the complex extinction dynamics. Our set of eight U-Pb dates from nonmarine sections in Southwest China provides the first comprehensive high-resolution temporal constraints on the EPME in terrestrial paleotropics.

Different age interpretation models yield different age assignments for Bed 68 (LAD of the organic-rich layer) at the Chahe section. The age of 251.804 + 0.078/−0.10 Ma ago generated from the MCMC model clearly constrains Bed 68 at the Chahe section to the earliest Triassic postdating the onset of the main marine extinction at the Meishan GSSP by 141 ± 94 ka (table S4 and fig. S7). In comparison, the weighted mean age of 251.884 ± 0.052 Ma ago for Bed 68 is a bit older and overlaps with the PTB, but it still postdates the onset of the main marine extinction by 61 ± 61 ka (table S4 and Fig. 2B). The moderately rich plant fossils did not disappear until ~0.7 m above Bed 68 at the Chahe section (*16*), further supporting a delayed collapse of the flora at the Chahe section. In the Lengqinggou section, the depositional age for the LAD of the organic-rich layer is constrained to the early Triassic under any age interpretation model (Fig. 2F, Table 1 and table S3). The collapse of the flora at the Lengqinggou section occurred 276 ± 104 ka after the onset of the main marine extinction based on the Bayesian MCMC model age. The depositional age at 251.81 + 0.13/−0.15 Ma ago of the ash bed in the uppermost Xuanwei Formation at the Yantang Mine section overlaps with the age of the marine PTB, but the dated ash bed is immediately overlain by a 30-cm-thick coal seam, suggesting that the base of the Kayitou Formation could be as young as early Triassic (Fig. 2C). Since the ages from the Mide section are obtained from the ash beds below the last organic-rich layer and all fall within the latest Permian or overlap with the marine PTB, the correlation of the Kayitou Formation at this location is informed only by fossil evidence and sequence stratigraphy (Fig. 2E). Abundant Triassic index fossil ammonoids *Ophiceras* sp., bivalves *Claraia* spp., and Triassic plants *Tomiostrobus* have been identified from the basal Kayitou Formation at the Mide section, establishing an early Triassic age (*14*, *15*).

The *Gigantopteris* flora in the last coal may have survived to the earliest Triassic at the Chuanyan and Zhongzhai sections in Southwest China (Fig. 2, G and H). The traditional PTB at the two sections was located on the lithological boundary between the Wangjiazhai and Feixianguan formations. The top of the Wangjiazhai Formation is characterized by the LAD of the coal seam with a diverse *Gigantopteris* flora bracketed by two ash beds (fig. S4). The Permian index conodont fossils *Clarkina meishanensis* and numerous Permian brachiopods have been identified from the sediments below the lower ash bed. The Triassic conodonts *Hindeodus parvus* and numerous Triassic bivalves have been identified in the bed between the two ash beds and immediately above the upper ash bed (*7*). These fossils suggest that the legacy CA-ID-TIMS ages in (*7*) are too old, and the last coal seam at the Chuanyan and Zhongzhai sections straddles the PTB. The collapse of the *Gigantopteris* flora at the two sections persisted to the earliest Triassic and thus postdated the onset of the main marine extinction.

The evident diachroneity of the LAD of organic-rich horizons in Southwest China (Fig. 2) is expected as coal-forming conditions reflect plant communities, as well as climatic and environmental conditions. Because plant species diversity at individual sections is susceptible to bias from preservation and lithofacies changes and because a limited number of tuffs are available for age determination, negative organic carbon isotope excursions (CIEs) have been taken as the primary stratigraphic correlation tool in this area (*20*–*22*). The organic carbon isotope ($\delta^{13}C_{org}$) values show different patterns between the terrestrial and marine sections, which could be attributed to complex local dynamics and fractionation, such as temperature, precipitation, and plant types, in addition to global changes in atmospheric $\delta^{13}C$ values (*33*). However, at a regional scale, the conditions are generally similar. This is confirmed by similar negative organic CIE patterns from different sections in Southwest China. The $\delta^{13}C_{org}$ values remained stable around −24‰ throughout the coal-bearing Xuanwei Formation before a rapid decline of 4 to 8‰ in the overlying Kayitou Formation and then reached a minimum value around −30‰ (Fig. 2) (*16*–*21*). Further support comes from the contemporaneity of the organic CIE and the Cu and Hg concentration spikes sourced from volcanic input at these sections (*18*, *20*–*22*, *34*).

The base of the Kayitou Formation as marked by the last coal seam records a younger transition from onshore to paralic sections based on the negative organic CIE correlations (Fig. 2). Specifically, the prominent negative CIE is found in the middle to upper part of the Kayitou

Formation at the terrestrial Guanbachong and Chahe sections, in the lower part of the Kayitou Formation at the transitional Chinahe and Mide sections, and on top of the Xuanwei Formation at the paralic Lengqinggou section (*16*–*20*). The correlation is also supported by the regional rapid retrogradation at the Chahe and Mide sections, which was documented in the uppermost part of the Xuanwei Formation above the dated ash beds at the Mide section, but in the basal part of the Kayitou Formation at the Chahe section (Fig. 2) (*14*). Thus, the ecosystem collapse may have occurred earlier in onshore areas like Guanbachong and Chahe. Although some typical Permian plant elements have been recovered from sediments above the last coal in the middle and upper part of the Kayitou Formation at some onshore sections, their diversity declined markedly, and the abundance of single species increased (*14*–*16*, *18*, *35*, *36*). Similarly, charcoals in the last coal bed at the top of the Xuanwei Formation at the paralic Lengqinggou section represent a monospecific assemblage during the extinction interval with extremely low diversity but high abundance (*19*).

Our high-precision U-Pb geochronology suggests temporal decoupling of the terrestrial and marine extinctions in paleotropical South China. The decline of the paleotropical rainforest occurred after the onset of the main marine extinction. The date from the top of the Xuanwei Formation at the Chahe section constrains the terrestrial crisis in Southwest China to at least 61 ± 61 ka after the onset of the main marine extinction. More sufficient evidence comes from the U-Pb geochronology at the Lengqinggou section, as well as the fossil records from the Mide, Chuanyan, and Zhongzhai sections, constraining the rainforest extinction to the early Triassic (Fig. 2). The collapse of the terrestrial ecosystem led to intensive soil erosion (*16*, *37*). The delayed tropical rainforest extinction was supported by a greater increase of terrestrial input after the main marine event in the earliest Triassic, which reached its peak following the final collapse of the tropical rainforest (*38*, *39*). Besides, unlike the brief marine extinction, the collapse of the terrestrial ecosystem lasted for a relatively long period, which started from the onshore areas, then progressed to the transitional and finally to the paralic areas in the earliest Triassic. According to the dates from the Chahe and Lengqinggou sections, the collapse of the tropical rainforest in Southwest China lasted for ~135 or ~215 ka depending on different age interpretation models (Fig. 2 and fig. S7). The final elimination of the Cathaysian rainforest in Southwest China across the marginal environment evidently lagged behind the marine EPME, postdating the end of the main marine event (Bed 28 at the Meishan GSSP) by 211 ± 103 ka (table S4). Conifers and ferns did not rediversify until the upper part of the Feixianguan Formation (*35*), as constrained by the depositional age of 251.509 + 0.085/−0.095 Ma ago from the lower Feixianguan Formation at the Lengqinggou section.

Latitudinal diachroneity of the terrestrial EPME

Previous work has shown that the marine ecosystem collapse was brief and globally synchronous and was embedded in a long-term interval of global environmental degradation. The onset of the main marine extinction has been constrained to the *Clarkina meishanensis* and equivalent conodont zones (*40*–*43*), which was calibrated to 251.945 ± 0.033 Ma ago at the Meishan GSSP (*3*) (table S4), 251.984 ± 0.031 (*44*) or 251.939 ± 0.031 Ma ago (*4*) at the extended Penglaitan section, and 251.939 ± 0.031 Ma ago at the Dongpan section (*44*) in South China.

Evidence suggests that ecosystem collapse in terrestrial regions took place diachronously with high-latitude terrestrial ecosystems declining before the main pulse of the marine extinction (Fig. 5). CA-ID-TIMS geochronology from the Sydney Basin in eastern Australia has indicated that the austral Permian *Glossopteris* forest ecosystem collapsed, and the peat accumulation terminated at 252.31 ± 0.07 Ma ago, predating the marine extinction by ~370 ka (*9*, *10*). The EPME in the Karoo Basin of South Africa is defined by a turnover from the *Daptocephalus* tetrapod assemblage zone (AZ) to *Lystrosaurus* AZ (*13*). The CA-ID-TIMS date of 252.24 ± 0.11 Ma ago from the basal part of the *Lystrosaurus* AZ suggests that the vertebrate transition occurred ~300 ka earlier than the main marine event (*11*). A survey of biotic diversity across Siberia did not reveal a sudden Permian-Triassic extinction, probably due to the relatively low resolution (*12*). Rather, at the well-studied Babyi Kamen section in the Kuznetsk Basin, Siberia, the coal seams disappeared at the boundary between the Tailugan and Maltsev formations at 252.764 ± 0.055 Ma ago, ~800 ka before the marine event. A notable reduction in nonmarine animals occurred shortly after 252.302 ± 0.090 Ma ago near the base of the Maltsev Formation (table S4) (*12*).

Although high-precision geochronological research on the EPME in terrestrial middle paleolatitudes has been inadequate, some important clues for the extinction timeline in those regions have come to light. In southern Tibet, the deforestation has been recorded at the base of the palynological assemblage of *Reduviasporonites catenulatus*, which is constrained to the latest Permian by gastropod and ammonoid fossils (*45*, *46*). The deforestation was followed by a changeover from regression to rapid transgression (*47*). The onset of this rapid transgression was placed in the conodont zone of *C. yini* below the onset of the main marine extinction in the latest Permian (*4*) (Fig. 5, D and G). In the Ordos Basin, North China, no *Gigantopteris* flora or Paleozoic-style pareiasaurs have been reported after 252.21 ± 0.15 Ma ago (*48*, *49*), but long-term aridity in this region (*50*, *51*) is believed to have increased the bias in the fossil records from the Signor-Lipps effect. The negative organic CIE and enhanced chemical weathering during the beginning of the rapid transgression soon after 252.21 ± 0.15 Ma ago mark the onset of the EPME in North China (*48*, *52*, *53*), which may have been coincident with the main marine event (Fig. 5E). Therefore, the limited available evidence suggests that the terrestrial middle-latitude ecosystems collapsed during the latest Permian and may have slightly postdated those in high latitudes. Our U-Pb geochronology together with fossil evidence suggests that the paleotropical EPME on land postdated the onset of the main marine event.

In summary, high-resolution geochronology suggests temporal decoupling of the terrestrial and marine extinctions. The terrestrial ecosystem collapsed diachronously with latitude over a ~1-Ma period, which began in high latitudes, progressed to middle latitudes, and finally to the tropics (Fig. 6). Besides, the collapse of the terrestrial ecosystems usually took a longer period and was followed by a long survival interval, in contrast to the rapid marine extinction (Fig. 5). In eastern Australia, elements of the *Glossopteris* flora persisted for another ~210 ka after the main deforestation (*10*). Similarly, in South Africa, *Glossopteris* leaves survived into the lower Katberg Formation above the main tetrapod turnover (*54*). Distinctive late Permian pollen taxa occur sporadically above the rapid decline in East Greenland (*8*). In South Tibet and the Salt Range (Pakistan), a degradation of the Permian conifers and pteridosperm plant communities was observed at the base of the *Reduviasporonites catenulatus* palynological assemblage, but the most dramatic palynofloral turnover took place in the earliest Triassic based on the ammonoid and conodont fossils (*47*, *55*). In Southwest China, the *Gigantopteris* flora persisted for another ~135 or ~215 ka in the paralic zones after their collapse in onshore areas.

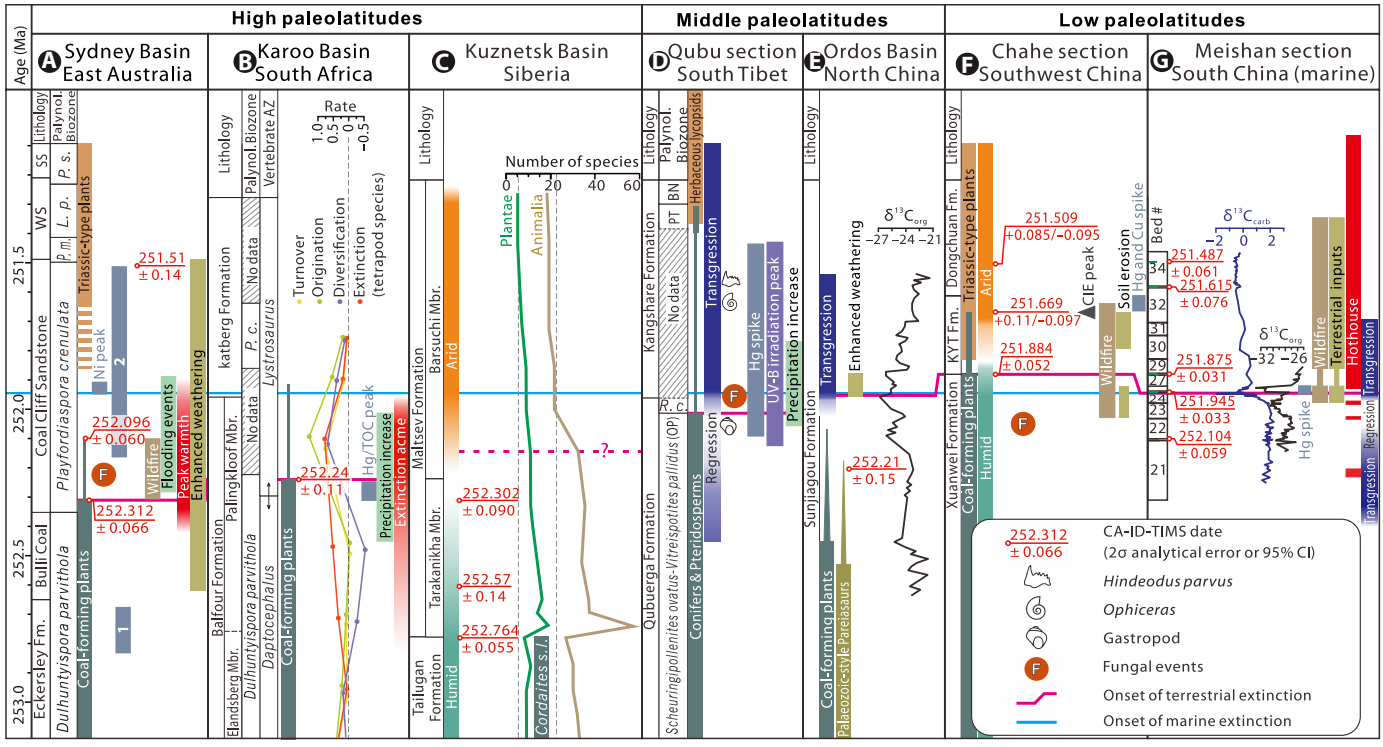

Fig. 5. Global correlation of the EPME. The correlation is mainly based on the high-precision U-Pb geochronology from (*3*, *9*–*12*, *49*), table S4, and this study. The geological and biological events from the Sydney Basin (*6*, *9*, *10*, *56*), Karoo Basin (*6*, *11*, *13*, *54*, *65*), Kuznetsk Basin (*12*), South Tibet (*47*, *69*), Ordos Basin (*48*, *52*, *53*), Southwest China (*14*, *16*, *21*, *37*), and the Meishan GSSP (*4*, *7*, *39*, *59*) were integrated on the basis of the high-resolution age model. Abbreviations: Palynol., Palynological; AZ, assemblage zone; Fm., Formation; Mbr., Member; KYT, Kayitou; *P. c.*, *Playfordiaspora crenulate*; *P. m.*, *Protohaploxypinus microcorpus*; *L. p.*, *Lunatisporites pellucidus*; *P. s.*, *Protohaploxypinus samoilovichii*; *R. c.*, *Reduviasporonites catenulatus*; *PT*, *Endosporites papillatus*–*Pinuspollenites thoracatus*; *BN*, *Lundbladispora brevicula*–*Densoisporites nejburgii*.

Possible triggers of terrestrial EPME

Evidence for long-term environmental degradation in marine realms before the marine EPME has been accumulating (*4*). The degradation in terrestrial realms began even earlier (*9*, *56*), which may explain the long-term decline in floral and faunal species richness during the earlier stages of the terrestrial ecosystem degradation in the late Permian (*12*, *13*, *35*). However, the diachroneity of the terrestrial extinction suggests a need for further exploration of the proximal extinction drivers. The large-scale volcanism and the related combustion of coals and evaporites may have caused massive injection of greenhouse gases, sulfates, and toxic volatiles into the atmosphere, which could have been fatal to terrestrial life through elevated temperatures, increased drought and seasonality, ozone shield depletion, and acid rains. Latitudinal variations in the impacts of elevated temperatures and depleted ozone shield appear to match the temporal pattern described earlier.

Community Earth System Model (CESM) simulations during the EPME reveal substantial polar amplification of an end-Permian temperature increase in middle-high latitudes, almost twice that of low latitudes (Fig. 6), with land areas warming more than the oceans (*57*, *58*). The paleo-temperature profiles suggest that the pronounced temperature elevation in terrestrial high latitudes predated those in marine paleotropics by more than 300 ka (*56*, *59*), whereas the relatively gentle temperature increases in the tropics may have been blurred by uncertainties in oxygen isotopic analyses. Polar amplification has also been reported in Paleogene and modern times (*60*, *61*). The more intensive warming in terrestrial high latitudes may have contributed to the earlier ecosystem collapse. In addition, the Permian Earth system model simulations suggest that the injection of greenhouse gases increased water vapor in high latitudes but decreased humidity in most middle latitudes and subtropics (*58*, *62*). Similar precipitation changes in modern climate observations and simulations have been reported (*63*, *64*). The geological evidence during the Permian-Triassic transition is consistent with the simulation results, recording precipitation spikes in mid-high latitudes (*10*, *47*, *53*, *56*, *65*) and enhanced seasonal aridity in paleotropics (*19*, *66*). However, despite the decreasing moisture in equatorial regions, the precipitation there remained higher than in high latitudes (*62*), which may have contributed to the delayed collapse of the Cathaysian *Gigantopteris* flora in the tropics. Increased precipitation in some terrestrial regions may have allowed the persistence of some Permian elements into the survival interval.

We also expect diachroneity in terrestrial ecosystem collapse reflecting latitudinal variation in ozone depletion. The presence of malformed pollen grains and increased deforestation during the EPME have been interpreted as indicators of ozone shield weakening (*67*–*69*). The CESM simulation reveals more intensive ozone reduction at high latitudes due to the release of halocarbons from SLIP (*70*), which may have initiated the earlier terrestrial ecological failure. However, halocarbons produced through contact metamorphism during the earliest Triassic intrusive phase of the SLIP are thought to have the strongest impact on ozone depletion (*71*, *72*). Thus, the direct release of halogens from the late Permian eruptive phase may have been insufficient to extensively damage the ozone layer. Substantial SO_2

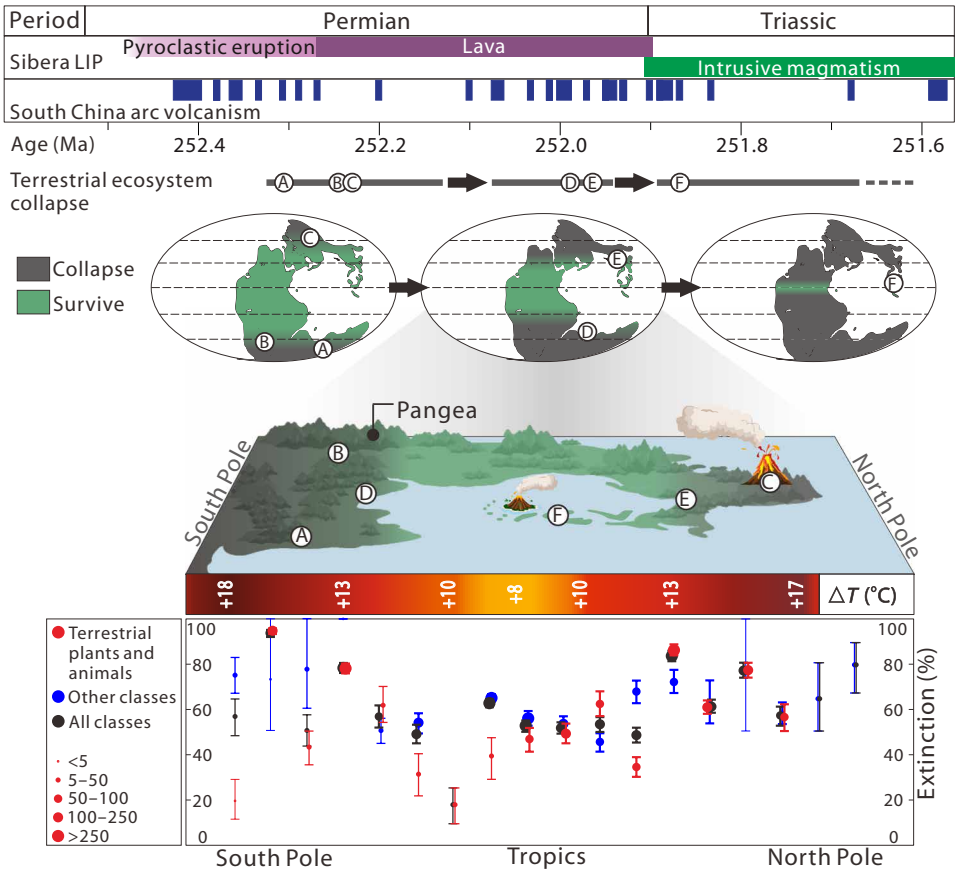

Fig. 6. Schematic illustration of the terrestrial EPME process. South China volcanic episodes are extracted from the ash bed records at Meishan (*3*), Penglaitan (*4*), and sections in this study. The emplacement timeline for Siberian LIP is modified from (*5*). Marked locations on maps are the same as those in Fig. 1. Horizontal schematic bars show the changes in land surface temperature (*58*). The latitudinal end-Permian genus extinction pattern is generated from bootstrap analyses based on data from Changhsingian to Induan in PBDB. Vertical bars show the confidence interval with 10 to 90% quantile ranges.

production from the Siberian Traps may have also contributed to the formation of the mutated spores. Furthermore, the flora diversified at the earliest Triassic in Siberia during the intrusive phase of the SLIP (*73*), suggesting that ozone reduction may have played a less important role compared to global warming in the EPME.

The more degraded high-latitude living conditions may have contributed to higher extinction rates based on the estimated genus extinction rates from data in the PBDB (Fig. 4). A similar pattern in latitudinal extinction intensity has been reported in marine realms, with possible control from variations in warming and the attendant anoxia in oceans (*57*). In addition to latitudinal variation in temperature elevation and possible ozone depletion, the impacts of degradation can vary depending on specific ecosystems, resulting in a protracted terrestrial extinction spanning approximately 1 Ma. Different terrestrial regions are characterized by local ecosystems that have adapted to specific environmental conditions. Plants and animals at high latitudes occupied a disappearing climatic niche and likely lacked a refuge during the deterioration, especially during the rapid warming. They may have been less tolerant of ecological changes and were the earliest to be eliminated. Higher resilience in tropical communities may have reflected higher species diversity and more complex food webs. Greater resilience allowed survival during the end-Permian catastrophe in the tropics, contributing to a delayed collapse in Southwest China. Yet, the delayed onset and short duration of the marine extinction could be attributed to several features, the ocean's vast size, its ability to absorb and distribute heat, and its complex circulation patterns. These factors could contribute to its greater resilience and stability during the degradation compared to the terrestrial ecosystems. However, once the marine ecosystem reaches a threshold that exceeds its buffering capacity and disrupts the balance, it can collapse immediately due to these same features.

Environmental decay during the late Permian had a major impact on the Cathaysian *Gigantopteris* flora including a decline in species richness (*35*) to the point where a single event could trigger its collapse. The large-scale, frequent felsic volcanism near the South China Block may have forced the ecosystem past this threshold. The felsic volcanism during the earliest Triassic is coincident with the final paleotropical ecosystem collapse in Southwest China and distributed widely in South China and nearby Tethyan regions (*20*, *21*, *74*–*76*). The coeval eruptions of the Siberian Traps may have contributed to the environmental degradation, but they continued for at least 500 ka into the early Triassic (*4*). The flora in the Tunguska Basin diversified at the beginning of the Triassic, suggesting that the emplacement of the Siberian Traps during that interval may have been insufficient to

eliminate the flora (*73*). The foregoing also raises questions about whether the SLIP was the sole cause of the EPME. The emplacement of the SLIP has been the most widely hypothesized trigger of the terrestrial and marine EPME since the early 1990s due to their temporal coincidence (*3*, *5*). However, sediments related to felsic volcanism developed extensively along the convergent margins of southern Pangea and around the Tethyan Ocean during the Permian-Triassic transition (*21*, *43*, *75*–*77*) (Fig. 1), introducing another possible stressor for the EPME. Mercury spikes during this interval have been reported globally and are thought to be derived from the SLIP (*6*), but they are not correlative between different sections based on the high-resolution geochronologic framework presented here, which could be generated from different stages of the SLIP or affected by local sedimentological processes (Fig. 5). It is also possible that they were generated from more proximal volcanic activities. Therefore, further study is needed to reappraise the impacts of the various types of volcanisms in different regions on the proximal environmental perturbations during the EPME.

MATERIALS AND METHODS

Zircon U-Pb analyses and data reduction

The samples for the U-Pb geochronological study were on the order of 2 to 5 kg in weight. They were processed by soaking in water for 48 hours, followed by complete liquefaction in a blender and clay removal in a sonic dismembrator device (*78*). Heavy-mineral concentrates were achieved through step-wise magnetic as well as high-density liquid separation techniques. The final zircon selection was carried out under a binocular microscope. Most samples contained mixed populations of zircons ranging from subrounded to multifaceted prisms. The prismatic or acicular zircon grains containing elongate glass (melt) inclusions parallel to their long axis are shown to represent the youngest population of zircons in the samples and were targeted for our analyses (fig. S5).

The selected zircon grains were pretreated by a chemical abrasion procedure modified from (*79*), which involved thermal annealing at 900°C for 60 hours, followed by partial dissolution in 29 M HF inside high-pressure Parr vessels at 210°C for 11.5 to 12 hours. The partially dissolved grains were fluxed alternately with dilute HNO_3 and 6 M HCl in 3 ml of Savillex perfluoroalkoxy (PFA) vials, on an 80°C hot plate, and in an ultrasonic bath, each for 1 hour. The grains were rinsed with Millipore water after every ultrasonic step to remove the leachates. The thoroughly rinsed grains were spiked with the EARTHTIME ET535 mixed ^{205}Pb-^{233}U-^{235}U tracer before complete dissolution in 29 M HF at 210°C for 45 to 48 hours. The dissolved aliquots were dried down on a hot plate and redissolved in 6 N HCl in high-pressure Parr vessels at 180°C overnight. The sample solutions were then converted from 6 to 3 N HCl by drying down and redissolution. The dissolved U and Pb were chemically purified using 50-μl columns of AG1X-8 anion-exchange resin. The eluted U and Pb were dried down with H_3PO_4 and then redissolved in a silica gel emitter solution and loaded onto a zone-refined outgassed Re filament.

The U-Pb isotopic ratios were measured on an Isotopx X62 multicollector thermal ionization mass spectrometer equipped with a Daly photomultiplier ion counting system at the Massachusetts Institute of Technology Isotope Laboratory. Pb isotopes were measured as monoatomic ions on a single ion counter and were corrected for a mass-dependent isotope fractionation of 0.18 ± 0.04% per atomic mass unit (2σ). U isotopes were measured as UO_2^{++} ions simultaneously on three Faraday collectors, while subjected to a within-run mass fractionation correction using the $^{233}U/^{235}U$ ratio of the tracer solution and a predicted sample $^{238}U/^{235}U$ ratio of 137.818 ± 0.045 (*80*). An oxide correction based on an independently determined $^{18}O/^{16}O$ ratio of 0.00205 ± 0.00005 was also applied to the measured U isotopic ratios. Initial Th/U disequilibrium was corrected using radiogenic ^{208}Pb and a magma Th/U ratio of 2.8.

Data reduction was carried out using the Tripoli and ET_Redux algorithms (*81*, *82*). Uncertainties are reported as 2σ in table S1. A total of 69 single-zircon grains from the eight samples were analyzed to estimate the eruptive ages by the conventional weighted mean $^{206}Pb/^{238}U$ model as well as the Bayesian MCMC algorithm of (*27*). Preferred age interpretations based on different models have been discussed in the Supplementary Materials (table S3 and fig. S6). Where appropriate, a second Bayesian MCMC rejection algorithm through the Bchron package was used to generate a depositional age model for the dated stratigraphy (Table 1 and fig. S8) (*29*). Since the data used in our interpretations were produced in the same laboratory using the same methods, we only used analytical errors in our age model, figures, and tables.

Extinction intensity estimation

The fossil occurrence data were downloaded from the PBDB selecting all fossil occurrence records from the Wuchiapingian to the whole Triassic (table S10). The extinction intensity was estimated by comparing the fossil occurrence records before and after the EPME. Since the PBDB is constructed on the basis of relative coarse time bins of a stage-level resolution, we are unable to improve the temporal resolution or adjust the timescale based on our dates. In most research, the PTB was often correlated to the EPME horizon in terrestrial sections due to a lack of high-precision isotopic dates or marine index fossils. The same principle has been applied to the terrestrial sediments in Southwest China in PBDB, with the Xuanwei and Kayitou formations recorded in the time bins of Changhsingian and Induan, respectively. Therefore, the extinction intensity was estimated by comparing the fossil occurrence records below and above the PTB.

The fossil occurrences in PBDB lacking a phylum or class assignment or lacking the paleolatitude information were excluded. Occurrences assigned to protistan groups were excluded. Occurrences assigned to the phylum or classes as entirely marine during the study interval (Anthozoa, Ascidiacea, Brachiopoda, Conodonta, Cephalopoda, etc.) were excluded, as were uncertain genus occurrences. Paleolatitudes of all occurrences were binned into 10° bands from 85°S to 85°N. The fossil data from (*12*) were included in the extinction and extirpation intensity estimation for the paleolatitude band of 65°N due to its small number of fossil collections in PBDB. The extinction intensity estimation is based on genera from three different taxonomic groupings: all classes together, the typical nonmarine classes (plants and terrestrial animals), and all other classes together (Fig. 4).

To see how dependent the latitudinal extinction rates are on the dataset and statistical methods, four methods have been used in the estimation. In the first method, the latitudinal extinction intensity is estimated by comparing the fossil occurrences from the Changhsingian with those from the Induan (Fig. 4A). In the second method, we applied a bootstrap analysis to compare the fossil occurrences between the Changhsingian with those in the Induan. All the occurrence data from the Changhsingian and Induan were resampled with replacement and with the same amount of raw data. Then, all the extinction and extirpation rates of different groups were recalculated at

each latitudinal zone based on the resampled data, and so were the occurrence numbers. This process was repeated 10,000 times. The mean values of all the indices were used as the analysis results, and their confidence intervals were generated within 10 to 90% quantile ranges (Fig. 4B). In the third method, we applied an updated version of the GF method proposed in (*31*, *32*) using dataset from the Wuchiapingian to Olenekian to estimate the extinction rates (Fig. 4D). This method uses four intervals spanning the boundary. Last, we estimated the extinction intensity by comparing the fossil occurrence records from the Changhsingian with those from the entire Triassic period (Fig. 4C). The comprehensive summary of each method is included in the Supplementary Materials.

Supplementary Materials

This PDF file includes:

Supplementary Text
Figs. S1 to S9
Tables S1 to S10
References

REFERENCES AND NOTES

1. D. M. Raup, J. J. Sepkoski, Mass extinctions in the marine fossil record. *Science* **215**, 1501–1503 (1982).
2. J. Dal Corso, H. J. Song, S. Callegaro, D. L. Chu, Y. D. Sun, J. Hilton, S. E. Grasby, M. M. Joachimski, P. B. Wignall, Environmental crises at the Permian-Triassic mass extinction. *Nat. Rev. Earth Environ.* **3**, 197–214 (2022).
3. S. D. Burgess, S. A. Bowring, S. Z. Shen, High-precision timeline for Earth's most severe extinction. *Proc. Natl. Acad. Sci. U.S.A.* **111**, 3316–3321 (2014).
4. S. Z. Shen, J. Ramezani, J. Chen, C. Q. Cao, D. H. Erwin, H. Zhang, L. Xiang, S. D. Schoepfer, C. M. Henderson, Q. F. Zheng, S. A. Bowring, Y. Wang, X. H. Li, X. D. Wang, D. X. Yuan, Y. C. Zhang, L. Mu, J. Wang, Y. S. Wu, A sudden end-Permian mass extinction in South China. *Geol. Soc. Am. Bull.* **131**, 205–223 (2019).
5. S. D. Burgess, S. A. Bowring, High-precision geochronology confirms voluminous magmatism before, during, and after Earth's most severe extinction. *Sci. Adv.* **1**, e1500470 (2015).
6. J. Shen, J. B. Chen, J. X. Yu, T. J. Algeo, R. M. H. Smith, J. Botha, T. D. Frank, C. R. Fielding, P. D. Ward, T. A. Mather, Mercury evidence from southern Pangea terrestrial sections for end-Permian global volcanic effects. *Nat. Commun.* **14**, 6 (2023).
7. S. Z. Shen, J. L. Crowley, Y. Wang, S. A. Bowring, D. H. Erwin, P. M. Sadler, C. Q. Cao, D. H. Rothman, C. M. Henderson, J. Ramezani, H. Zhang, Y. A. Shen, X. D. Wang, W. Wang, L. Mu, W. Z. Li, Y. G. Tang, X. L. Liu, L. J. Liu, Y. Zeng, Y. F. Jiang, Y. G. Jin, Calibrating the end-Permian mass extinction. *Science* **334**, 1367–1372 (2011).
8. R. J. Twitchett, C. V. Looy, R. Morante, H. Visscher, P. B. Wignall, Rapid and synchronous collapse of marine and terrestrial ecosystems during the end-Permian biotic crisis. *Geology* **29**, 351–354 (2001).
9. C. R. Fielding, T. D. Frank, S. McLoughlin, V. Vajda, C. Mays, A. P. Tevyaw, A. Winguth, C. Winguth, R. S. Nicoll, M. Bocking, J. L. Crowley, Age and pattern of the southern high-latitude continental end-Permian extinction constrained by multiproxy analysis. *Nat. Commun.* **10**, 385 (2019).
10. C. R. Fielding, T. D. Frank, A. P. Tevyaw, K. Savatic, V. Vajda, S. McLoughlin, C. Mays, R. S. Nicoll, M. Bocking, J. L. Crowley, M. Ghinassi, Sedimentology of the continental end-Permian extinction event in the Sydney Basin, eastern Australia. *Sedimentology* **68**, 30–62 (2021).
11. R. A. Gastaldo, S. L. Kamo, J. Neveling, J. W. Geissman, C. V. Looy, A. M. Martini, The base of the *Lystrosaurus* Assemblage Zone, Karoo Basin, predates the end-Permian marine extinction. *Nat. Commun.* **11**, 1428 (2020).
12. V. I. Davydov, E. V. Karasev, N. G. Nurgalieva, M. D. Schmitz, I. V. Budnikov, A. S. Biakov, D. M. Kuzina, V. V. Silantiev, M. N. Urazaeva, V. V. Zharinova, S. O. Zorina, B. Gareev, D. V. Vasilenko, Climate and biotic evolution during the Permian-Triassic transition in the temperate Northern Hemisphere, Kuznetsk Basin, Siberia, Russia. *Palaeogeogr. Palaeoclimatol. Palaeoecol.* **573**, 110432 (2021).
13. P. A. Viglietti, R. B. J. Benson, R. M. H. Smith, J. Botha, C. F. Kammerer, Z. Skosan, E. Butler, A. Crean, B. Eloff, S. Kaal, J. Mohoi, W. Molehe, N. Mtalana, S. Mtungata, N. Ntheri, T. Ntsala, J. Nyaphuli, P. October, G. Skinner, M. Strong, H. Stummer, F. P. Wolvaardt, K. D. Angielczyk, Evidence from South Africa for a protracted end-Permian extinction on land. *Proc. Natl. Acad. Sci. U.S.A.* **118**, e2017045118 (2021).
14. A. Bercovici, Y. Cui, M. B. Forel, J. X. Yu, V. Vajda, Terrestrial paleoenvironment characterization across the Permian-Triassic boundary in South China. *J. Asian Earth Sci.* **98**, 225–246 (2015).
15. J. X. Yu, J. Broutin, Z. Q. Chen, X. Shi, H. Li, D. L. Chu, Q. S. Huang, Vegetation changeover across the Permian-Triassic Boundary in Southwest China. Extinction, survival, recovery and palaeoclimate: A critical review. *Earth Sci. Rev.* **149**, 203–224 (2015).
16. H. Zhang, C. Q. Cao, X. L. Liu, L. Mu, Q. F. Zheng, F. Liu, L. Xiang, L. J. Liu, S. Z. Shen, The terrestrial end-Permian mass extinction in South China. *Palaeogeogr. Palaeoclimatol., Palaeoecol.* **448**, 108–124 (2016).
17. Y. Cui, A. Bercovici, J. X. Yu, L. R. Kump, K. H. Freeman, S. G. Su, V. Vajda, Carbon cycle perturbation expressed in terrestrial Permian-Triassic boundary sections in South China. *Glob. Planet. Change* **148**, 272–285 (2017).
18. D. L. Chu, S. E. Grasby, H. J. Song, J. D. Corso, Y. Wang, T. A. Mather, Y. Y. Wu, H. Y. Song, W. C. Shu, J. N. Tong, P. B. Wignall, Ecological disturbance in tropical peatlands prior to marine Permian-Triassic mass extinction. *Geology* **48**, 288–292 (2020).
19. Y. F. Cai, H. Zhang, Z. Feng, S. Z. Shen, Intensive wildfire associated with volcanism promoted the vegetation changeover in Southwest China during the Permian-Triassic transition. *Front. Earth Sci.* **9**, 615–814 (2021).
20. X. D. Wang, P. A. Cawood, S. E. Grasby, L. S. Zhao, Z. Q. Chen, S. L. Wu, Y. G. Huang, Characteristics of Hg concentrations and isotopes in terrestrial and marine facies across the end-Permian mass extinction. *Glob. Planet. Change* **205**, 103592 (2021).
21. H. Zhang, F. F. Zhang, J. B. Chen, D. H. Erwin, D. D. Syverson, P. Ni, M. Rampino, Z. Chi, Y. F. Cai, L. Xiang, W. Q. Li, S. A. Liu, R. C. Wang, X. D. Wang, Z. Feng, H. M. Li, T. Zhang, H. M. Cai, W. Zheng, Y. Cui, X. K. Zhu, Z. Q. Hou, F. Y. Wu, Y. G. Xu, N. Planavsky, S. Z. Shen, Felsic volcanism as a factor driving the end-Permian mass extinction. *Sci. Adv.* **7**, eabh1390 (2021).
22. D. L. Chu, J. D. Corso, W. C. Shu, H. J. Song, P. B. Wignall, S. E. Grasby, B. v. d. Schootbrugge, K. Q. Zong, Y. Y. Wu, J. N. Tong, Metal-induced stress in survivor plants following the end-Permian collapse of land ecosystems. *Geology* **49**, 657–661 (2021).
23. G. J. Retallack, Permian-triassic life crisis on land. *Science* **267**, 77–80 (1995).
24. G. J. Retallack, J. J. Veevers, R. Morante, Global coal gap between Permian-Triassic extinction and Middle Triassic recovery of peat-forming plants. *Geol. Soc. Am. Bull.* **108**, 195–207 (1996).
25. J. X. Yu, H. M. Li, S. X. Zhang, F. Q. Yang, Q. L. Feng, Timing of the terrestrial Permian-Triassic boundary biotic crisis: Implications from U-Pb dating of authigenic zircons. *Sci. China Ser. D Earth Sci.* **51**, 1633–1645 (2008).
26. J. Wang, L. Y. Shao, H. Wang, B. Spiro, D. Large, SHRIMP zircon U-Pb ages from coal beds across the Permian-Triassic boundary, eastern Yunnan, southwestern China. *J. Palaegeogr.* **7**, 117–129 (2018).
27. C. B. Keller, B. Schoene, K. M. Samperton, A stochastic sampling approach to zircon eruption age interpretation. *Geochem. Perspecti. Lett.* **8**, 31–35 (2018).
28. B. Schoene, M. P. Eddy, K. M. Samperton, C. B. Keller, G. Keller, T. Adatte, S. F. R. Khadri, U-Pb constraints on pulsed eruption of the Deccan Traps across the end-Cretaceous mass extinction. *Science* **363**, 862–866 (2019).
29. J. Haslett, A. Parnell, A simple monotone process with application to radiocarbon-dated depth chronologies. *J. R. Stat. Soc. C.* **57**, 399–418 (2008).
30. J. Guex, B. Schoene, A. Bartolini, J. Spangenberg, U. Schaltegger, L. O'Dogherty, D. Taylor, H. Bucher, V. Atudorei, Geochronological constraints on post-extinction recovery of the ammonoids and carbon cycle perturbations during the Early Jurassic. *Palaeogeogr. Palaeoclimatol. Palaeoecol.* **267**, 483–275 (2012).
31. J. Alroy, Accurate and precise estimates of origination and extinction rates. *Paleobiology* **40**, 374–397 (2014).
32. J. Alroy, A more precise speciation and extinction rate estimator. *Paleobiology* **41**, 633–639 (2015).
33. Z. G. Rao, W. K. Guo, J. T. Cao, F. X. Shi, H. Jiang, C. Z. Li, Relationship between the stable carbon isotopic composition of modern plants and surface soils and climate: A global review. *Earth Sci. Rev.* **165**, 110–119 (2017).
34. J. Shen, J. Yu, J. Chen, T. J. Algeo, G. Xu, Q. Feng, X. Shi, N. J. Planavsky, W. Shu, S. Xie, Mercury evidence of intense volcanic effects on land during the Permian-Triassic transition. *Geology* **47**, 1117–1121 (2019).
35. Z. Xu, J. Hilton, J. X. Yu, P. B. Wignall, H. F. Yin, Q. Xue, W. J. Ran, H. Li, J. Shen, F. S. Meng, End Permian to Middle Triassic plant species richness and abundance patterns in South China: Coevolution of plants and the environment through the Permian-Triassic transition. *Earth Sci. Rev.* **232**, 104136 (2022).
36. Z. Feng, H. B. Wei, R. H. Ye, Q. Sui, X. D. Gou, Y. Guo, L. J. Liu, S. L. Yang, Latest Permian Peltasperm plant from Southwest China and its Paleoenvironmental implications. *Front. Earth Sci.* **8**, 559430 (2020).
37. R. K. Biswas, K. Kaiho, R. Saito, L. Tian, Z. Q. Shi, Terrestrial ecosystem collapse and soil erosion before the end-Permian marine extinction: Organic geochemical evidence from marine and non-marine records. *Glob. Planet. Change* **195**, 103327 (2020).
38. S. C. Xie, R. D. Pancost, J. H. Huang, P. B. Wignall, J. X. Yu, X. Y. Tang, L. Chen, X. Y. Huang, X. L. Lai, Changes in the global carbon cycle occurred as two episodes during the Permian–Triassic crisis. *Spec. Pap. Geol. Soc. Am.* **35**, 1083–1086 (2007).

39. S. C. Xie, T. J. Algeo, W. F. Zhou, X. Y. Ruan, G. M. Luo, J. H. Huang, J. X. Yan, Contrasting microbial community changes during mass extinctions at the Middle/Late Permian and Permian/Triassic boundaries. *Earth Planet. Sci. Lett.* **460**, 180–191 (2017).
40. D. X. Yuan, S. Z. Shen, C. M. Henderson, J. Chen, H. Zhang, H. Z. Feng, Revised conodont-based integrated high-resolution timescale for the Changhsingian Stage and end-Permian extinction interval at the Meishan sections, South China. *Lithos* **204**, 220–245 (2014).
41. D. X. Yuan, S. Z. Shen, C. M. Henderson, J. Chen, H. Zhang, Q. F. Zheng, H. C. Wu, Integrative timescale for the Lopingian (Late Permian): A review and update from Shangsi, South China. *Earth Sci. Rev.* **188**, 190–209 (2019).
42. J. Chen, S. Z. Shen, Y. C. Zhang, L. Angiolini, M. N. Gorgij, G. Crippa, W. Wang, H. Zhang, D. X. Yuan, X. H. Li, Y. G. Xu, Abrupt warming in the latest Permian detected using high-resolution in situ oxygen isotopes of conodont apatite from Abadeh, central Iran. *Palaeogeogr. Palaeoclimatol. Palaeoecol.* **560**, 109973 (2020).
43. J. Shen, J. B. Chen, T. J. Algeo, Q. L. Feng, J. X. Yu, Y. G. Xu, G. Z. Xu, Y. Lei, N. J. Planavsky, S. C. Xie, Mercury fluxes record regional volcanism in the South China craton prior to the end-Permian mass extinction. *Geology* **49**, 452–456 (2021).
44. B. Baresel, H. Bucher, M. Brosse, F. Cordey, G. D. Kuang, U. Schaltegger, Precise age for the Permian-Triassic boundary in South China from high-precision U-Pb geochronology and Bayesian age-depth modeling. *Solid Earth* **8**, 361–378 (2017).
45. S. Z. Shen, C. Q. Cao, C. M. Henderson, X. D. Wang, G. R. Shi, Y. Wang, W. Wang, End-Permian mass extinction pattern in the northern peri-Gondwanan region. *Palaeoworld* **15**, 3–30 (2006).
46. C. Zhang, H. Bucher, S. Z. Shen, Griesbachian and Dienerian (Early Triassic) ammonoids from Qubu in the Mt. Everest area, southern Tibet. *Palaeoworld* **26**, 650–662 (2017).
47. F. Liu, H. P. Peng, B. Bomfleur, H. Kerp, H. C. Zhu, S. Z. Shen, Palynology and vegetation dynamics across the Permian-Triassic boundary in southern Tibet. *Earth Sci. Rev.* **209**, 103278 (2020).
48. D. L. Chu, J. N. Tong, M. J. Benton, J. X. Yu, Y. F. Huang, Mixed continental-marine biotas following the Permian-Triassic mass extinction in South and North China. *Palaeogeogr. Palaeoclimatol. Palaeoecol.* **519**, 95–107 (2019).
49. W. W. Guo, J. N. Tong, Q. He, M. W. Hounslow, H. Y. Song, J. Dal Corso, P. B. Wignall, J. Ramezani, L. Tian, D. L. Chu, Late Permian-Middle Triassic magnetostratigraphy in North China and its implications for terrestrial-marine correlations. *Earth Planet. Sci. Lett.* **585**, 117519 (2022).
50. Q. Wu, J. Ramezani, H. Zhang, J. Wang, F. G. Zeng, Y. C. Zhang, F. Liu, J. Chen, Y. F. Cai, Z. S. Hou, C. Llu, W. Yang, C. M. Henderson, S. Z. Shen, High-precision U-Pb age constraints on the Permian floral turnovers, paleoclimate change and tectonics of the North China block. *Geology* **49**, 677–681 (2021).
51. Z. C. Zhu, H. W. Kuang, Y. Q. Liu, M. J. Benton, A. J. Newell, H. Xu, W. An, S. A. Ji, S. C. Xu, N. Peng, Q. G. Zhai, Intensifying aeolian activity following the end Permian mass extinction: Evidence from the Late Permian-Early Triassic terrestrial sedimentary record of the Ordos Basin, North China. *Sedimentology* **67**, 2691–2720 (2020).
52. Y. Y. Wu, J. N. Tong, T. J. Algeo, D. L. Chu, Y. Cui, H. Y. Song, W. C. Shu, Y. Du, Organic carbon isotopes in terrestrial Permian-Triassic boundary sections of North China: Implications for global carbon cycle perturbations. *Geol. Soc. Am. Bull.* **132**, 1106–1118 (2020).
53. Y. Cao, H. Y. Song, T. J. Algeo, D. L. Chu, Y. Du, L. Tian, Y. H. Wang, J. N. Tong, Intensified chemical weathering during the Permian-Triassic transition recorded in terrestrial and marine successions. *Palaeogeogr. Palaeoclimatol. Palaeoecol.* **519**, 166–177 (2019).
54. R. A. Gastaldo, S. L. Kamo, J. Neveling, J. W. Geissman, M. Bamford, C. V. Looy, Is the vertebrate-defined Permian-Triassic boundary in the Karoo Basin, South Africa, the terrestrial expression of the end-Permian marine event? *Geology* **43**, 939–942 (2015).
55. E. Schneebeli-Hermann, W. M. Kürschner, H. Kerp, B. Bomfleur, P. A. Hochuli, H. Bucher, D. Ware, G. Roohi, Vegetation history across the Permian–Triassic boundary in Pakistan (Amb section, Salt Range). *Gondw. Res.* **27**, 911–924 (2015).
56. T. D. Frank, C. R. Fielding, A. M. E. Winguth, K. Savatic, A. Tevyaw, C. Winguth, S. McLoughlin, V. Vajda, C. Mays, R. Nicoll, M. Bocking, J. L. Crowley, Pace, magnitude, and nature of terrestrial climate change through the end-Permian extinction in southeastern Gondwana. *Geology* **49**, 1089–1095 (2021).
57. J. L. Penn, C. Deutsch, J. L. Payne, E. A. Sperling, Temperature-dependent hypoxia explains biogeography and severity of end-Permian marine mass extinction. *Science* **362**, eaat1327 (2018).
58. B. A. Black, R. R. Neely, J.-F. Lamarque, L. T. Elkins-Tanton, J. T. Kiehl, C. A. Shields, M. J. Mills, C. Bardeen, Systemic swings in end-Permian climate from Siberian Traps carbon and sulfur outgassing. *Nat. Geosci.* **11**, 949–954 (2018).
59. J. Chen, S. Z. Shen, X. H. Li, Y. G. Xu, M. M. Joachimski, S. A. Bowring, D. H. Erwin, D. X. Yuan, B. Chen, H. Zhang, Y. Wang, C. Q. Cao, Q. F. Zheng, L. Mu, High-resolution SIMS oxygen isotope analysis on conodont apatite from South China and implications for the end-Permian mass extinction. *Palaeogeogr. Palaeoclimatol. Palaeoecol.* **448**, 26–38 (2016).
60. J. Cohen, J. A. Screen, J. C. Furtado, M. Barlow, D. Whittleston, D. Coumou, J. Francis, K. Dethloff, D. Entekhabi, J. Overland, J. Jones, Recent Arctic amplification and extreme mid-latitude weather. *Nat. Geosci.* **7**, 627–637 (2014).
61. J. E. Tierney, J. Zhu, M. Li, A. Ridgwell, G. J. Hakim, C. J. Poulsen, R. D. M. Whiteford, J. W. B. Rae, L. R. Kump, Spatial patterns of climate change across the Paleocene-Eocene Thermal Maximum. *Proc. Natl. Acad. Sci. U. S. A.* **119**, e2205326119 (2022).
62. C. J. Poulsen, D. Pollard, I. P. Montañez, D. Rowley, Late Paleozoic tropical climate response to Gondwanan deglaciation. *Geology* **35**, 771–774 (2007).
63. X. B. Zhang, F. W. Zwiers, G. C. Hegerl, F. H. Lambert, N. P. Gillett, S. Solomon, P. A. Stott, T. Nozawa, Detection of human influence on twentieth-century precipitation trends. *Nature* **448**, 461–465 (2007).
64. S. Solomon, G.-K. Plattner, R. Knutti, P. Friedlingstein, Irreversible climate change due to carbon dioxide emissions. *Proc. Natl. Acad. Sci. U. S. A.* **106**, 1704–1709 (2009).
65. G. J. Retallack, Multiple Permian-Triassic life crises on land and at sea. *Glob. Planet. Change* **198**, 103415 (2021).
66. Z. M. Yan, L. Y. Shao, I. J. Glasspool, J. Wang, X. T. Wang, H. Wang, Frequent and intense fires in the final coals of the Paleozoic indicate elevated atmospheric oxygen levels at the onset of the end-permian mass extinction event. *Int. J. Coal Geol.* **207**, 75–83 (2019).
67. H. Visscher, C. V. Looy, M. E. Collinson, H. Brinkhuis, J. H. A. van Konijnenburg-van Cittert, W. M. Kürschner, M. A. Sephton, Environmental mutagenesis during the end-Permian ecological crisis. *Proc. Natl. Acad. Sci. U. S. A.* **101**, 12952–12956 (2004).
68. J. P. Benca, I. A. P. Duijnstee, C. V. Looy, UV-B-induced forest sterility: Implications of ozone shield failure in Earth's largest extinction. *Sci. Adv.* **4**, e1700618 (2018).
69. F. Liu, H. P. Peng, J. E. A. Marshall, B. H. Lomax, B. Bomfleur, M. S. Kent, W. T. Fraser, P. E. Jardine, Dying in the sun: Direct evidence for elevated UV-B radiation at the end-Permian mass extinction. *Sci. Adv.* **9**, eabo6102 (2023).
70. B. A. Black, J.-F. Lamarque, C. A. Shields, L. T. Elkins-Tanton, J. T. Kiehl, Acid rain and ozone depletion from pulsed Siberian Traps magmatism. *Geology* **42**, 67–70 (2014).
71. H. Svensen, N. Schmidbauer, M. Roscher, F. Stordal, S. Plank, Contact metamorphism, halocarbons, and environmental crises of the past. *Environ. Chem.* **6**, 466–471 (2009).
72. D. J. Beerling, M. Harfoot, B. Lomax, J. A. Pyle, The stability of the stratospheric ozone layer during the end-Permian eruption of the Siberian Traps. *Philos. Trans. A. Math. Phys. Eng. Sci.* **365**, 1843–1866 (2007).
73. V. I. Davydov, E. V. Karasev, The influence of the Permian-Triassic magmatism in the Tunguska Basin, Siberia on the Regional Floristic Biota of the Permian-Triassic transition in the region. *Front. Earth Sci.* **9**, doi.org/10.3389/feart.2021.635179 (2021).
74. X. D. Wang, P. A. Cawood, H. Zhao, L. S. Zhao, S. E. Grasby, Z. Q. Chen, L. Zhang, Global mercury cycle during the end-Permian mass extinction and subsequent Early Triassic recovery. *Earth Planet. Sci. Lett.* **513**, 144–155 (2019).
75. T. Y. Zhao, T. J. Algeo, Q. L. Feng, J. W. Zi, G. Z. Xu, Tracing the provenance of volcanic ash in Permian-Triassic boundary strata, South China: Constraints from inherited and syn-depositional magmatic zircons. *Palaeogeogr. Palaeoclimatol. Palaeoecol.* **516**, 190–202 (2019).
76. O. Edward, A. N. Paul, H. Bucher, C. Vérard, T. Adatte, J. E. Sonke, U. Schaltegger, T. Vennemann, Timing and provenance of volcanic fluxes around the Permian-Triassic boundary mass extinction in South China: U-Pb zircon geochronology, volcanic ash geochemistry and mercury isotopes. *Geochem. Geophys. Geosyst.* **24**, e2023GC010912 (2023).
77. N. Riel, E. Jaillard, J.-E. Martelat, S. Guillot, J. Braun, Permian-Triassic Tethyan realm reorganization: Implications for the outward Pangea margin. *J. S. Am. Earth Sci.* **81**, 78–86 (2018).
78. G. D. Hoke, M. D. Schmitz, S. A. Bowring, An ultrasonic method for isolating nonclay components from clay-rich material. *Geochem. Geophys. Geosyst.* **15**, 492–498 (2014).
79. J. M. Mattinson, Zircon U–Pb chemical abrasion ("CA-TIMS") method: Combined annealing and multi-step partial dissolution analysis for improved precision and accuracy of zircon ages. *Chem. Geol.* **220**, 47–66 (2005).
80. J. Hiess, D. J. Condon, N. McLean, S. R. Noble, $^{238}U/^{235}U$ systematics in terrestrial uranium-bearing minerals. *Science* **335**, 1610–1614 (2012).
81. J. F. Bowring, N. M. McLean, S. A. Bowring, Engineering cyber infrastructure for U-Pb geochronology: Tripoli and U-Pb_Redux. *Geochem. Geophys. Geosyst.* **12**, Q0AA19 (2011).
82. N. M. McLean, J. F. Bowring, S. A. Bowring, An algorithm for U-Pb isotope dilution data reduction and uncertainty propagation. *Geochem. Geophys. Geosyst.* **12**, Q0AA18 (2011).
83. R. Scotese, An atlas of phanerozoic paleogeographic maps: The seas come in and the seas go out. *Annu. Rev. Earth Planet. Sci.* **49**, 679–728 (2021).
84. V. Ivanov, S. B. Mukasa, V. S. Kamenetsky, M. Ackerson, E. I. Demonterova, B. G. Pokrovsky, N. V. Vladykin, M. V. Kolesnichenko, K. D. Litasov, D. A. Zedgenizov, Volatile concentrations in olivine-hosted melt inclusions from meimechite and melanephelinite lavas of the Siberian Traps Large Igneous Province: Evidence for flux-related high-Ti, high-Mg magmatism. *Chem. Geol.* **483**, 442–462 (2018).
85. C. Parnell, J. Haslett, J. R. M. Allen, C. E. Buck, B. Huntley, A flexible approach to assessing synchroneity of past events using Bayesian reconstructions of sedimentation history. *Quat. Sci. Rev.* **27**, 1872–1885 (2008).
86. H. Zhang, Z. Feng, J. Ramezani, S. Z. Shen, Comments on "Terrestrial Permian-Triassic boundary in southern China: New stratigraphic, structural and palaeoenvironment considerations" by Bourquin et al. (2018). *Palaeogeogr. Palaeoclimatol. Palaeoecol.* **506**, 254–256 (2018).

87. I. Wendt, C. Carl, The statistical distribution of the mean squared weighted deviation. *Chem. Geol.* **86**, 275–285 (1991).
88. B. Schoene, U–Th–Pb geochronology, in *Treatise on Geochemistry* (Elsevier, ed. 2, 2014), pp. 341–378.
89. H. Jaffey, K. F. Flynn, L. E. Glendenin, W. C. Bentley, A. M. Essling, Precision measurement of half-lives and specific activities of 235U and 238U. *Phys. Rev. C* **4**, 1889–1906 (1971).

Acknowledgments: We thank I. Bennett for expeditious zircon separation at the Massachusetts Institute of Technology. We thank the three anonymous reviewers for constructive comments and suggestions to improve the manuscript. **Funding:** This work was supported by the National Natural Science Foundation (grant nos. 42293280, 42261144668, 42250104, 42102020, and 42325201), the Guangdong Basic and Applied Basic Research Foundation (2023A1515010896), the PI Project of Southern Marine Science and Engineering Guangdong Laboratory (Guangzhou) (GML2022006), the Yunnan Province Science and Technology Department (202302AO370014), and the Key Research Program of the Institute of Geology and Geophysics, Chinese Academy of Sciences (IGGCAS-201905). **Author contributions:** Supervision: S.-z.S. Conceptualization: S.-z.S. Investigation: S.-z.S., H.Z., Q.W., J.R., Z.F., L.-y.S., and Y.-f.C. Methodology: Q.W., J.R., S.-h.Z., S.-z.S., and H.Z. Formal analysis: Q.W., J.R., and S.-h.Z. Writing—original draft: Q.W. under the guidance of S.-z.S. Writing—review and editing: Q.W., S.-z.S., D.H.E., J.R., H.Z., Y.-g.X., Z.F., and F.-f.Z. **Competing interests:** The authors declare that they have no competing interests. **Data and materials availability:** All data needed to evaluate the conclusions in the paper are present in the paper and/or the Supplementary Materials.

Submitted 15 May 2023
Accepted 29 December 2023
Published 31 January 2024
10.1126/sciadv.adi7284